Ultrafast Excited-State Dynamics of V_3O_5 as a Signature of a Photoinduced Insulator-Metal Phase Transition

Nardeep Kumar, Armando Rúa, Junqiang Lu, Félix Fernández, and Sergiy Lysenko*
Department of Physics, University of Puerto Rico, Mayaguez, Puerto Rico 00681, USA
(Received 23 March 2017; published 1 August 2017)

The ultrafast elastic light scattering technique is applied to reveal the strong nonlinearity of V_3O_5 associated with a photoinduced insulator-metal phase transition. Observation of time-domain relaxation dynamics suggests several stages of structural transition. We discuss the nonequilibrium processes in V_3O_5 in terms of photoinduced melting of a polaronic Wigner crystal, coalescence of V-O octahedra, and photogeneration of acoustical phonons in the low-T and high-T phases of V_3O_5. A molecular dynamics computation supports experimentally observed stages of V_3O_5 relaxation dynamics.

DOI: 10.1103/PhysRevLett.119.057602

Vanadium oxides show exotic optical, electronic, magnetic, and structural properties, including metal-insulator phase transitions due to specific behavior of d electrons [1]. Among these oxides, V_3O_5 undergoes an insulator-to-metal transition (IMT) at the highest temperature, $T_c \sim 430$ K [2]. V_3O_5 is the first member of the Magnéli series V_nO_{2n-1}, $n = 3, 4, \ldots, 9$ [3], and is the only known vanadium oxide other than VO_2 [4] that shows a phase transition above room temperature. Its initial monoclinic symmetry does not change through the transition point, except for a slight variation of lattice parameters [5,6]. With T_c above room temperature, V_3O_5 is a very promising candidate for new optoelectronic applications. It has been shown that IMT can be triggered by various degrees of freedom, such as temperature [2,7], electric field [8], and pressure [9,10]. However, the evidence of IMT in V_3O_5 induced by light has not been demonstrated.

In this Letter, we report on the observation of excited-state dynamics in V_3O_5. Applying an ultrafast light scattering technique, we show that the complete formation a of new phase occurs within 1 ps. The phase transition dynamics depends on the level of optical excitation and shows several stages, interpreted as order-disorder structural transition triggered by photoinduced melting of a polaronic Wigner crystal. A photoacoustic strain can produce coherent oscillations of the light scattering signal. The ultrafast structural dynamics was modeled by molecular dynamics computation.

High-quality 120 nm thick V_3O_5 film was grown on a SiO_2 substrate by reactive dc magnetron sputtering from a vanadium target with 99.95% purity. The sample was characterized by x-ray diffraction (XRD). All sharp XRD peaks [Fig. 1(a)] are assigned to the low-T monoclinic phase of V_3O_5, according to Ref. [11].

Ultrafast pump-probe scattering measurements were performed with an ultrafast scatterometer in reflection geometry described elsewhere [12]. Amplified 130 fs pulses with central wavelength $\lambda = 800$ nm are split into a pump beam and a frequency-doubled probe beam ($\lambda = 400$ nm). Scattered light was collected within the front hemisphere by an elliptical mirror and focused on a silicon photodetector. The temperature T of the sample was controlled by a Peltier module. The penetration depth of insulating V_3O_5 was measured as 30 nm for $\lambda = 800$ nm and 25 nm for $\lambda = 400$ nm. Therefore, a relaxation dynamic was monitored for a uniformly excited sample within the penetration depth of the probe.

Figure 1(b) shows the temperature dependence of the sample resistivity ρ, static scattering signal, and

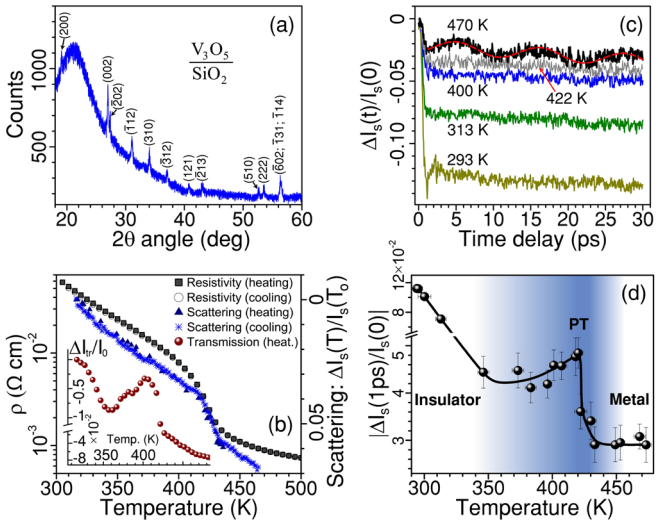

FIG. 1. (a) The XRD pattern of V_3O_5/SiO_2 film. (b) Resistivity ρ and relative change $\Delta I_s(T)/I_s(T_0)$ of static scattering intensity $I_s(T)$ as a function of sample temperature, $\Delta I_s(T) = I_s(T) - I_s(T_0)$. The inset shows the relative change of transmittance $\Delta I_{tr}(T)/I_0$, where $\Delta I_{tr}(T) = I_{tr}(T) - I_0$, $I_{tr}(T)$ is transmitted and I_0 is incident intensity of light; $\lambda = 800$ nm. (c) Differential scattering $\Delta I_s(t)/I_s(0)$ versus time t at different temperatures of the sample; $F = 14\,\mathrm{mJ/cm^2}$. $\Delta I_s(t) = I_s(t) - I_s(0)$. Dashed line is the fit by Eq. (1) at $T = 470$ K. (d) Photoinduced change of scattering signal at 1 ps delay versus temperature.

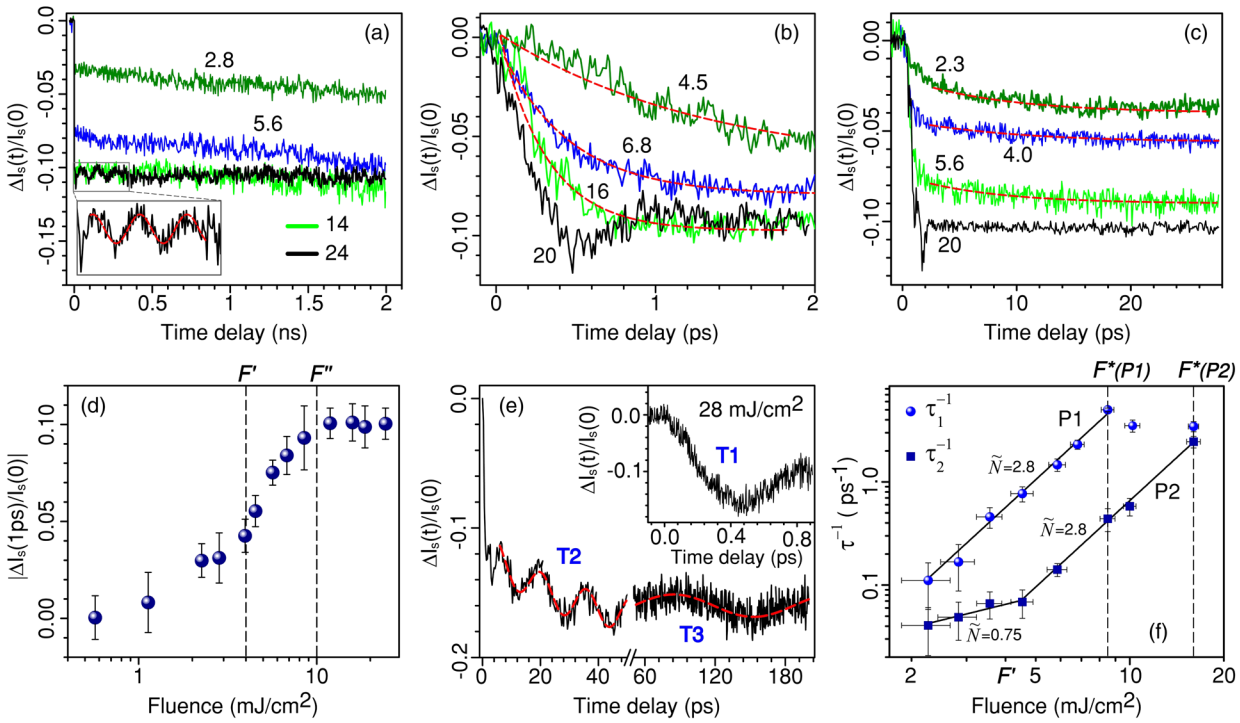

FIG. 2. Transient differential scattering signal $\Delta I_s(t)/I_s(0)$ within (a) 2 ns (b) 2 ps, and (c) 27 ps time scale. Numbers specify the laser pump fluence in mJ/cm^2. Dashed lines are the fit by Eq. (2) for process P1 in (b) and P2 in (c). (d) The magnitude $|\Delta I_s(1\text{ ps})/I_s(0)|$ of the scattering signal measured at 1 ps delay. (e) Differential signal $\Delta I_s(t)/I_s(0)$ at $F = 28$ mJ/cm^2. Dashed lines are fits by Eq. (1). (f) Characteristic relaxation rates for processes P1 and P2. Solid lines are fits by Eq. (3).

transmittance. From 415 to 435 K these dependencies show a sharp change due to IMT, defining a transition temperature $T_c \sim 425$ K, which agrees with the known value for V_3O_5 [13]. Moreover, a noticeable dip in the transmittance signal was observed at ~360 K. This behavior shows that the monoclinic structure starts preparing for the IMT at ~65 K below T_c, which is consistent with the literature for this compound [14,15].

Figure 1(c) shows the transient light scattering $\Delta I_s(t)/I_s(0)$ measured with a pump fluence $F = 14$ mJ/cm^2 at different sample temperatures, ranging from 293 to 470 K. For every temperature the signal is composed of two distinct processes: a noticeable decrease of the signal within ~2 ps, followed by its relatively small change during several picoseconds afterwards. Moreover, pronounced oscillations appear in the metallic phase of V_3O_5 at $T = 470$ K. Additional details are provided in the Supplemental Material [16].

The rapid change of scattering signal magnitude $|\Delta I_s(1\text{ ps})/I_s(0)|$ measured at 1 ps delay at different temperatures [Fig. 1(d)] shows a noticeable decrease at 360 K, followed by a relatively small rise until ~420 K. This behavior is similar to that of the transmittance [inset in Fig. 1(b)], showing that the nonlinear optical (NLO) properties of V_3O_5 have a specific feature at 360 K. Within the interval from 420 to 450 K the signal shows a sharp drop due to thermally induced IMT. However, the metallic V_3O_5 also shows well-resolved transient NLO response with a nearly constant signal above 450 K.

The evolution of transient scattering on relatively long 2 ns time scale [Fig. 2(a)] and quantitative analysis of the heat deposited to the film allows estimating a rise of the film temperature upon photoexcitation. Here we use the heat capacity and the latent heat [200 cal/mole (3594 J/kg)] of V_3O_5 obtained in Refs. [19,20], respectively. Above ~270 K, the heat capacity increases linearly from 688 to 760 J/(K kg), as the temperature changes from 293 to 350 K. For 120 nm V_3O_5 film, the measurements of the reflection coefficient ($R = 11\%$) and transmission ($T = 2.4\%$) yield the absorption coefficient of 0.866. For reliable estimation of the V_3O_5 temperature in the insulating phase, we assume that the only photon energy of 1.55 eV $- E_g$ is transferred to the lattice. Since the band gap of V_3O_5 is $E_g = 0.6$ eV [7], the estimation shows that at least 60% of absorbed energy is transferred to the lattice after electron-phonon relaxation. Taking into account a density of the film, $\rho = 4.69$ g/cm^3 [21], simple calorimetric calculations show that the fluence of 12 mJ/cm^2 is enough to heat the entire film from room temperature $T_0 = 293$ K to $T_c = 425$ K and to produce complete thermal phase transition. At $F = 14$ mJ/cm^2, the film temperature exceeds the T_c point on ~30 K, and at $F = 24$ mJ/cm^2 on ~125 K.

The 2 ns time scale is sufficiently long to convert the energy of photoexcited electrons into the heat via

electron-phonon and phonon-phonon scattering. The photoinduced dynamics in Figs. 2(a)–2(c) at $F = 14$, 16, 20, and 24 mJ/cm^2 is accompanied by significant increase of the temperature well above T_c. Moreover, the relative change of the scattering signal for these excitations is the same. As shown in Fig. 2(a) for $F = 14$ and 24 mJ/cm^2, there is no noticeable relaxation that can be observed within the 2 ns time scale (except of acoustic oscillations at $F = 24$ mJ/cm^2). Therefore, it can be argued that the V_3O_5 film at $F \geq 14$ mJ/cm^2 is already in the metallic state within the observed 2 ns time scale, at least due to thermally induced phase transition. The only transient dynamics that can be observed on a shorter time scale is the relaxation within ~1 ps [see the signal evolution for $F = 16$ and 20 mJ/cm^2 in Figs. 2(b) and 2(c)]. From 1 ps and up to the maximally observed 2 ns time scale, the signal is constant and corresponds to the same level of $\Delta I_s(t)/I_s(0) = -0.1$ for any excitation fluence above 16 mJ/cm^2. This yields the conclusion that the optical excitation with $F \geq 16$ mJ/cm^2 produces complete insulator-metal phase transition in a V_3O_5 film on the time scale as short as ~1 ps.

New features appear as the pump fluence reaches 24 mJ/cm^2. Figure 2(a) shows oscillations of the signal within 500 ps with a period of 120 ps. Additional measurements of this NLO dynamics at $F = 28$ mJ/cm^2 show that the transient scattering response can be rationalized as a three-step process, labeled as T1, T2, and T3 in Fig. 2(e). The initial process T1 is associated with the generation of a photoexcited metallic state within 1 ps. This is followed by excitation of coherent acoustic phonons (process T2), which decay after ~50 ps into mode T3. The acoustic mode T3 corresponds to the oscillations shown in the inset of Fig. 2(a).

The pronounced oscillations within ~50 ps [process T2 in Fig. 2(e)] compare well with oscillations that appear in the metallic phase of V_3O_5 at $T = 470$ K [Fig. 1(c)] and manifest the excited metallic state. The transient scattering signal in Fig. 2(e) within ~50 ps can be described by the equation

$$\frac{\Delta I_s(t)}{I_s(0)} = A_0 + A_1 \sin[2\pi f(t - t_c)] + A_2 e^{-t/\tau_R}, \quad (1)$$

where A_0, A_1, and A_2 are fitting amplitude constants, f is the vibrational frequency, t_c is the time of complete electron-phonon relaxation during the IMT, and τ_R is the relaxation time of process T2. The exponential term accounts for the exponential decay background. The acoustic mode T2 after ~50 ps decays into mode T3 with the signal $\Delta I_s(t)/I_0(0) = A_0 + A_1 \sin(2\pi f t)$. Fitting of $\Delta I_s(t)/I_s(0)$ to two oscillatory components gives a period of 15 ps ($f = 67$ GHz) for mode T2, and a period of 120 ps ($f = 8.3$ GHz) for mode T3.

According to Thomsen *et al.* [22], the absorption of the pump pulse with $\lambda = 800$ nm excites a longitudinal acoustic wave within the penetration depth of the film, $\zeta = 30$ nm. This wave reflects several times from the boundary of the photoexcited metallic phase of V_3O_5 within ζ thickness, resulting in the oscillations of the $\Delta I_s(t)/I_s(0)$ signal. The speed of sound v_s and period of oscillations T_S are related as $v_s = 2\zeta/T_S$ [22]. Using the period of oscillations of $T_S = 15$ ps, the speed of sound comes out to be $v_s = 4 \times 10^3$ m/s. After ~50 ps the acoustic pulse penetrates farther into the film volume and reflects already from the film boundary at the substrate, producing lower-frequency oscillations with $T_S = 120$ ps. For this case, the relation between v_s and period T_S is $v_s = 4d/T_S$ [23–25], where d is the film thickness. The measured period of oscillations of $T_S = 120$ ps and $d = 120$ nm also give the value of the speed of sound $v_s = 4 \times 10^3$ m/s.

The light-induced IMT monitored within 2 ps [Fig. 2(b)] and 27 ps time scales [Fig. 2(c)] at $F < 20$ mJ/cm^2 shows two distinctive relaxation components that can be approximated by the function

$$\frac{\Delta I_s(t)}{I_s(0)} = A_0 + A_1 \exp(-t/\tau_1) + A_2 \exp(-t/\tau_2), \quad (2)$$

where τ_1 and τ_2 are characteristic relaxation times. The relaxation rates τ_1^{-1} and τ_2^{-1} obtained are plotted in Fig. 2(f) and assigned to two relaxation processes designated as P1 and P2. In a log-log graph, the relaxation rates show linear dependencies on pump fluence. The P2 process shows two components separated by fluence $F = 4.5$ mJ/cm^2. The relaxation rate of each process can be fitted as

$$\tau^{-1} = \gamma F^{\tilde{N}}, \quad (3)$$

where γ and $\tilde{N}$ are fitting constants. Although the phase transition of V_3O_5 shows features of a first-order transition [7,14], the lattice transformation occurs within a relatively broad temperature range and almost without a hysteresis, altering electrical and optical properties of the material below and above T_c [Fig. 1(b)]. As shown in Ref. [13], such critical behavior of V_3O_5 is likely originated from an order-disorder phase transition, which is second order. In the case of light-induced transition, increasing pump fluence reduces the activation energy E_a of each process involved in the IMT. The relaxation rate is proportional to the probability of the process and can be written as

$$\tau^{-1} = \tau_0^{-1} \exp(-E_a/k_B T), \quad (4)$$

where τ_0 is the shortest relaxation time and k_B is the Boltzmann constant. Equations (2) and (3) yield the dependence of the energy E_a on pump fluence,

$$E_a = -\tilde{N} k_B T \ln(F/F^*), \quad (5)$$

where F^* is the pump fluence at which the shortest relaxation time τ_0 is detected. $F^*(\mathrm{P1}) = 8.5$ mJ/cm^2 and $F^*(\mathrm{P2}) = 16$ mJ/cm^2 for the processes P1 and P2. The fitting constant $\tilde{N}$ defines the slope of τ_1^{-1} and τ_2^{-1} in Fig. 2(f) and can be interpreted as the constant that characterizes the number of atoms and number of degrees of freedom involved in the IMT process. Thus, $\tilde{N} = 0.75$ for the first component of P2, and $\tilde{N} = 2.8$ for P1 and for the second component of P2. The fact that slopes of $\tau_1^{-1}(F)$ and $\tau_2^{-1}(F)$ for $F > 4.5$ mJ/cm^2 are equal indicates that P1 and P2 represent similar relaxation processes in V_3O_5. On the other hand, P1 and P2 could also represent different stages of a single pathway of IMT, and this is a subject for further investigations. As the pump fluence further increases to 16 mJ/cm^2, processes P1 and P2 merge, and complete IMT occurs in less than 1 ps.

Processes P1 and P2 both compare with the magnitude of the scattering signal $|\Delta I_s(1\ \mathrm{ps})/I_s(0)|$ measured at 1 ps delay for a series of pump fluences F [Fig. 2(d)]. The monotonic rise of $|\Delta I_s(1\ \mathrm{ps})/I_s(0)|$ changes at $F' = 4$ mJ/cm^2 and at $F'' = 10$ mJ/cm^2. It is interesting to note that the fluence F'' is fairly close to the upper limit $F^*(\mathrm{P1})$ for process P1, and the fluence F' is close to the fluence where the slope $\tilde{N}$ of $\tau_2^{-1}(F)$ changes [$F = 4.5$ mJ/cm^2 in Fig. 2(f)]. The different slope of $\tau_2^{-1}(F)$ below and above $F = 4.5$ mJ/cm^2 indicates different relaxation dynamics in process P2. Overall, the NLO response of V_3O_5 undergoes a sharp qualitative change starting from $F' = 4$ mJ/cm^2. Therefore, this fluence was assigned as the threshold for the IMT.

Although strong interelectron correlations play a crucial role in stabilizing the insulating phase, the IMT of V_3O_5 is not considered as a pure Mott-Hubbard-type transition [7]. In the insulating phase, the V_3O_5 unit cell consists of four independent V-O octahedrons, referenced as V(11), V(12), V(21), and V(22) [21]. The V(11) octahedron hosts a V^{4+} ion. V(12), V(21), and V(22) all host V^{3+} ions. The holes are localized within the V(11) octahedron [21] and can be considered as small polarons [7,10]. As a result, V(11) is the smallest and the most distorted octahedron. In this system the IMT can be induced by altering the spatial segregation of the charges [7].

The low-T insulating phase of V_3O_5 originates from strong electron correlations. It is very likely that the correlations result in Wigner crystallization of small polarons [7,10]. This process significantly decreases conductivity and results in ordering of ions of different valence in the monoclinic lattice (space group $P2/c$; Fig. 2 in Supplemental Material [16]) with unit cell parameters $a = 9.859$ Å, $b = 5.0416$ Å, $c = 6.991$ Å, and angle $\beta = 109.478°$ [5].

The concept of polaronic Wigner crystal is very important for the understanding of photoinduced IMT in V_3O_5. In this scenario, photogeneration of a dense electron-hole plasma produces screening of electron correlations to the level when Coulomb interaction cannot provide segregation and localization of charges. As a result, the polaronic crystal melts into noncorrelated polaronic states. Additional charge transfer may occur between V^{3+} and V^{4+} ions. This process significantly increases the mobility of polarons, resulting in lattice instability followed by structural transition. It is very likely that the photoinduced melting of a polaronic crystal is sufficiently fast and occurs on a femtosecond time scale as a part of process P1 [Figs. 2(b) and 2(f)].

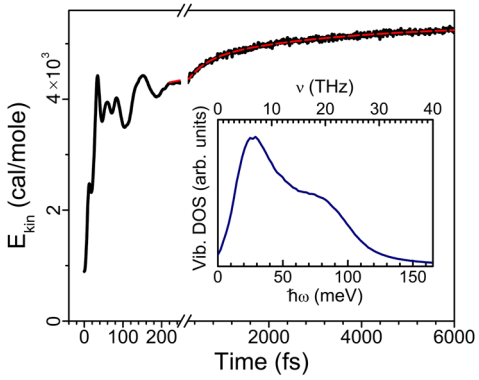

FIG. 3. Kinetic energy relaxation for V_3O_5 lattice. A double exponential fit (dashed line) yields two relaxation times: $\tau_1 = 405$ fs and $\tau_2 = 3.1 \times 10^3$ fs. Inset: Vibrational density of states of all V_3O_5 atoms.

According to Refs. [21,26], the IMT phase transition of V_3O_5 occurs as a coalescence of V(11) and V(12) octahedra into V(1), hosting a mixture of V^{3+} and V^{4+} ions, and also as a coalescence of V(21) and V(22) octrahedra into V(2), hosting only V^{3+} ions. It is likely that for the IMT triggered by femtosecond light pulses, these two coalescence processes take place at different rates.

In order to gain deeper insight into the ultrafast structural dynamics of V_3O_5, we modeled lattice relaxation by the semiclassical computational method of molecular dynamics (MD) using the QUANTUMWISE software package [27]. Figure 3 shows the adiabatic relaxation of kinetic energy for a V_3O_5 cluster of 16,384 atoms at $T = 298$ K. The computation of MD applied the ReaxFF reactive force field simulation method, which does not include correlation effects, but retains nearly the accuracy of quantum mechanical calculations [28]. Therefore, MD of V_3O_5 can be considered as a fairly close approximation of lattice relaxation of a real V_3O_5 lattice obtained from XRD experiment [5] to some other structure when correlation effects are suppressed by photoexcitation. While the metallic phase of V_3O_5 is still a correlated metal, here we assume that these correlations are much weaker as compared to the case of insulating V_3O_5.

The relaxation dynamics of kinetic energy E_{kin} in Fig. 3 reveals significant instability of the V_3O_5 lattice. Thus, E_{kin} increases by 3.5 kcal/mole in less than 100 fs, followed by

further nearly exponential growth with two distinct characteristic relaxation times: $\tau_1 = 405$ fs and $\tau_2 = 3.1 \times 10^3$ fs. These values compare well with experimentally observed relaxation times of initial drop ($\tau_1 = 405$ fs, process P1) and posterior picosecond relaxation ($\tau_2 = 4.4 \times 10^3$ fs, process P2) of the scattering signal at $F = 6.8$ mJ/cm^2 [see Fig. 2(f)]. Thus, computed relaxation dynamics strongly support the presence of experimentally observed processes P1 and P2 [Figs. 2(b), 2(c), and 2(f)]. These two processes could be associated with coalescence of vanadium octahedra. The initial rise of E_{kin} within 100 fs can be associated with melting of polaronic crystal in the absence of electron correlations.

The inset in Fig. 3 shows the vibrational density of states calculated for all atoms of the V_3O_5 cluster. MD computation shows a broad resonance with a maximum at ~6.5 THz. However, in the present study, lattice oscillations at THz frequencies were not resolved.

In summary, the ultrafast scattering data reveal noticeable transient nonlinearity of V_3O_5 associated with IMT. The phase transition dynamics can be interpreted in terms of an order-disorder structural transition triggered by photoinduced screening of electron correlations followed by melting of polaronic Wigner crystal and coalescence of V-O octahedra. A noticeable photoacoustic response of V_3O_5 was revealed at temperatures above and also below T_c. The molecular dynamics computation supports the model for the experimentally observed relaxation dynamics.

The authors gratefully acknowledge support from the U.S. Army Research Laboratory and the U.S. Army Research Office under Contract No. W911NF-15-1-0448.

*sergiy.lysenko@upr.edu

[1] M. Imada, A. Fujimori, and Y. Tokura, Rev. Mod. Phys. **70**, 1039 (1998).
[2] N. Bogdanova and C. Aria, Sov. J. Gen. Chem. **30**, 3 (1960).
[3] U. Schwingenschlögl and V. Eyert, Ann. Phys. (Berlin) **13**, 475 (2004).
[4] F. Morin, Phys. Rev. Lett. **3**, 34 (1959).
[5] E. Terukov, D. Khomskii, and F. Chudnovskii, Sov. Phys. JETP **46**, 1160 (1977).
[6] H. Keer and J. Honig, Mater. Res. Bull. **12**, 277 (1977).
[7] F. Chudnovskii, E. Terukov, and D. Khomskii, Solid State Commun. **25**, 573 (1978).
[8] B. Fisher, L. Patlagan, K. Chashka, C. Makarov, and G. Reisner, Appl. Phys. Lett. **109**, 103501 (2016).
[9] V. Sidorov, A. Waśkowska, and D. Badurski, Solid State Commun. **125**, 359 (2003).
[10] L. Baldassarre, A. Perucchi, E. Arcangeletti, D. Nicoletti, D. Di Castro, P. Postorino, V. A. Sidorov, and S. Lupi, Phys. Rev. B **75**, 245108 (2007).
[11] Powder Diffraction File 72-0977, International Centre for Diffraction Data, PA, USA, http://www.icdd.com/index.htm.
[12] S. Lysenko, F. Fernández, A. Rúa, and H. Liu, J. Appl. Phys. **114**, 153514 (2013).
[13] V. Andreev and V. Klimov, Phys. Solid State **53**, 2424 (2011).
[14] S. Åsbrink and S.-H. Hong, Nature (London) **279**, 624 (1979).
[15] S.-H. Hong and S. Åsbrink, J. Appl. Crystallogr. **14**, 43 (1981).
[16] See Supplemental Material at http://link.aps.org/supplemental/10.1103/PhysRevLett.119.057602 for additional figures and accompanying text, which includes Refs. [17,18].
[17] G. Kresse and J. Hafner, Phys. Rev. B **47**, 558 (1993).
[18] J. P. Perdew, K. Burke, and M. Ernzerhof, Phys. Rev. Lett. **77**, 3865 (1996).
[19] B. F. Griffing, S. P. Faile, and J. M. Honig, Phys. Rev. B **21**, 154 (1980).
[20] E. I. Terukov, F. A. Chudnovskii, W. Reichelt, H. Oppermann, W. Brückner, H.-P. Brückner, and W. Moldenhauer, Phys. Status Solidi A **37**, 541 (1976).
[21] S. Åsbrink, Acta Crystallogr. Sect. B **36**, 1332 (1980).
[22] C. Thomsen, H. T. Grahn, H. J. Maris, and J. Tauc, Phys. Rev. B **34**, 4129 (1986).
[23] C. Thomsen, J. Strait, Z. Vardeny, H. J. Maris, J. Tauc, and J. J. Hauser, Phys. Rev. Lett. **53**, 989 (1984).
[24] A. C. Diebold, *Handbook of Silicon Semiconductor Metrology* (CRC Press, New York, 2001).
[25] E. Abreu *et al.*, arXiv:1701.05531.
[26] S.-H. Hong and S. Åsbrink, Acta Crystallogr. Sect. B **38**, 713 (1982).
[27] Atomistix ToolKit, QuantumWise A/S, http://www.quantumwise.com.
[28] K. Chenoweth, A. C. Van Duin, and W. A. Goddard, J. Phys. Chem. A **112**, 1040 (2008).